Influence of mechanical hardening and numerical setup on liquid rocket engine combustion chamber life perdition

DOI: 10.13009/EUCASS2025-500
11TH EUROPEAN CONFERENCE FOR AERONAUTICS AND SPACE SCIENCES (EUCASS)

Influence of mechanical hardening and numerical setup on liquid rocket engine combustion chamber life perdition

Matteo Crachi[⋆†], *Marco Pizzarelli*[•], *Raffaella Sesana*[⋆], *Cristiana Delprete*[⋆]

[⋆] *DIMEAS, Polytechnic of Turin University, Turin, Italy*
[•] *Italian Space Agency, Rome, Italy*
matteo.crachi@polito.it
[†]Corresponding author

Abstract

The thrust chamber of high-performance bipropellant liquid rocket engines is a critical component in reusable launch vehicles, as it directly influences engine efficiency, structural integrity, and operational lifespan. To withstand the extreme thermal and mechanical loads experienced during operation, these chambers employ a regenerative cooling system, which serves a dual purpose: it mitigates the severe thermal stresses on the chamber walls by dissipating heat while simultaneously preheating the fuel or oxidizer before injection, enhancing overall propulsion efficiency.
Ensuring the durability and reusability of thrust chambers necessitates accurate thermo-mechanical life prediction. However, estimating their operational lifespan is challenging due to several factors, including the lack of reliable simplified specimen characterization, uncertainties in heat flux prediction, and the difficulty in selecting an appropriate plasticity model for computational analysis. These challenges often lead to an overestimation of service life, necessitating extensive and costly test campaigns until structural failure. Such experimental validation remains essential for refining numerical thermo-mechanical models and improving predictive capabilities. This study aims to investigate the influence of numerical modeling assumptions on the life prediction of copper-based liquid rocket engine combustion chambers using a commercial structural finite element method (FEM) solver. Specifically, a comparative analysis is conducted between different modeling approaches, including 2D plane strain, 2D generalized plane strain, and 3D generalized plane strain formulations. These approaches are evaluated in conjunction with a second-order Chaboche-Voce hardening model, incorporating both kinematic and isotropic hardening effects. The study places particular emphasis on the impact of low-cycle fatigue and ratcheting damage, which are critical failure mechanisms in cyclic thermal loading conditions.
To validate the numerical models, experimental data from the Space Shuttle Main Engine (SSME) subscale cylindrical thrust chamber test campaign at NASA's former Lewis Research Center (LeRC) are used as a reference case study. The LeRC plug thrust chambers provide a unique opportunity for hardware-representative low-cycle thermal fatigue evaluation, offering essential benchmark data, including precise temperature measurements obtained from multiple-depth intrusive thermocouples and recorded cycle-to-failure counts. By leveraging this rare experimental dataset, the study aims to establish validated thermal boundary conditions and enhance the predictive accuracy of thermo-mechanical analyses for reusable liquid rocket engine thrust chambers.

1. Introduction

1.1 Liquid rocket engine regenerative cooled combustion chambers

The thrust chamber of a bipropellant regenerative cooled liquid rocket engine is a key component in modern reusable launch vehicles, playing a vital role in delivering sustained propulsion under extreme conditions. One of the primary design challenges associated with such systems lies in managing the intense thermal loads encountered during operation. To address this, regenerative cooling systems (RCS) are commonly employed. These systems serve a dual purpose: they cool the chamber walls exposed to high-temperature combustion gases and simultaneously preheat the propellants-thereby improving overall engine efficiency.

DOI: 10.13009/EUCASS2025-500

The recurring thermal cycles experienced by the thrust chamber, particularly during multiple engine restarts, can result in low-cycle thermal fatigue, which significantly influences the operational life of the component. Consequently, accurate life prediction is essential not only for ensuring mission safety and engine reliability but also for enabling refurbishment and reuse strategies that reduce operational costs. Effective life prediction hinges on the integration of high-fidelity thermal and mechanical models into the design process. Regeneratively cooled thrust chambers typically consist of an inner wall made from high thermal conductivity metal alloys (to maximize heat transfer), and an outer jacket fabricated from high-strength super-alloy (to provide mechanical support). This material combination, coupled with the differing wall thicknesses and local thermal gradients, introduces substantial internal strains, posing significant challenges to the structural integrity of the chamber (Figure 1).

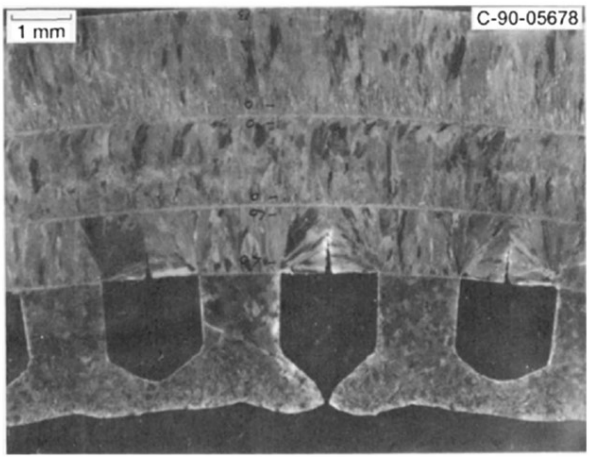

Figure 1: Common liquid rocket engine regenerative cooling inner wall channel 'dog house' failure.[3]

Current predictive methodologies often suffer from limited accuracy, primarily due to the lack of standardized, simplified test specimens that can reliably replicate the complex thermomechanical conditions found in operational engines. As a result, repeated full-scale hot-fire testing remains the most reliable approach for evaluating thrust chamber life. However, this method is both costly and time-intensive. To mitigate these challenges, numerical simulation has become a valuable tool. Despite the inherent uncertainties associated with simulating the behavior of materials under extreme and cyclic loading conditions, finite element methods (FEM) are widely used for life estimation.

In this context, the present study explores the influence of different numerical set-up models on the predicted mechanical response of a regeneratively cooled thrust chamber. Using a commercial finite element solver, the authors investigate the behavior of the chamber under cyclic loading, with a particular focus on low-cycle fatigue and plastic strain evolution. The SN40 sub-scale plug chamber developed by NASA Lewis Research Center is selected as the reference test case, due to the availability of extensive experimental data.

1.2 NASA Lewis Research Center Combustion chambers

As part of the Space Shuttle Main Engine (SSME) development program, the NASA Lewis Research Center (LeRC) conducted an extensive series of experimental investigations focused on the low-cycle thermal fatigue behavior of regeneratively cooled liquid rocket engine thrust chambers. These tests, dating back to the 1970s, were carried out on sub-scale demonstrator hardware referred to as "plug chambers." The aim was to generate reliable data for understanding failure mechanisms in the thrust chamber wall and to support lifetime prediction methodologies for reusable engine components.[4]

The plug chambers were deliberately designed to replicate the essential thermal and mechanical phenomena occurring in a full-scale SSME, particularly in the region exposed to extreme thermal and pressure loads. Each assembly consisted of an injector head, a water-cooled centerbody (which created the axisymmetric convergent-divergent nozzle contour), and a cylindrical thrust chamber segment (Figure 2). The primary goal was to evaluate the performance and durability of different copper-based materials for the hot gas side wall liner, given their critical role in ensuring thermal conductivity and structural integrity under cyclic loading.

In these experiments, various candidate materials were assessed for their suitability, including Amzirc, Narloy-Z, and Oxygen-Free High Conductivity (OFHC) copper for the milled inner liner. Electro-formed copper was used as the closeout layer, completing the regenerative cooling channel. These combinations allowed researchers to compare material responses under identical loading conditions.

DOI: 10.13009/EUCASS2025-500

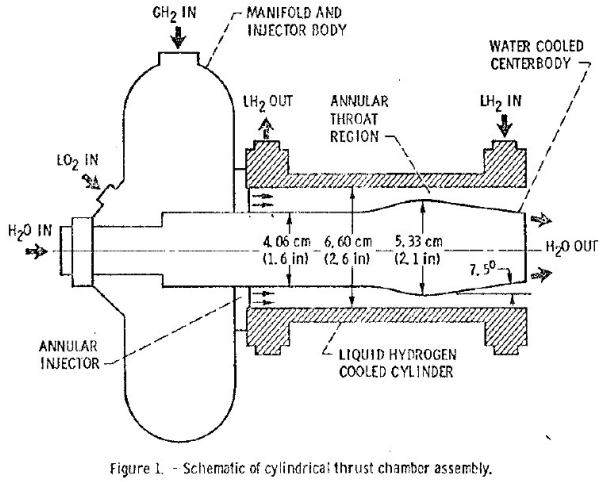

Figure 2: Plug chamber assembly. Image from.[4]

Among the tested configurations, the plug-chamber labeled SN40 was selected as the reference case for the present study due to the availability of comprehensive thermal[4] and material characterization data,[1] including detailed thermocouple measurements and cycling history. The SN40 unit employed a milled inner liner made from Amzirc alloy and an electro-formed copper closeout, creating a representative sandwich structure consistent with practical engine combustion chambers.

The experimental campaign for SN40 involved repeated firing cycles, each lasting approximately 3.5 seconds - 1.7 seconds for the ignition and steady-state burn, followed by 1.8 seconds of post-burn cooling. The chamber operated at a nominal pressure of 40 bar,[4] with liquid hydrogen continuously flowing through the cooling channels to maintain wall temperatures within the target range. The testing continued until thermal fatigue led to observable damage and eventual failure in the cylindrical wall section. A representation of the experimental single cycle is reported in Figure 3.

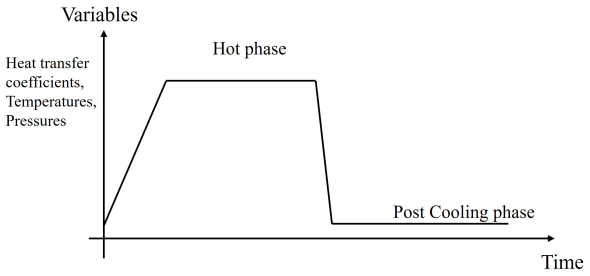

Figure 3: Typical single LeRC Plug chambers typical cycle history.

To monitor temperature distribution during operation, thermocouples were embedded at various radial positions within the cooling ribs near the throat region-known to experience the highest thermal loads. Specifically, two thermocouples were installed in separate ribs: one near the hot gas wall (0.89 mm from the surface) and the other at a mid-wall location (1.78 mm from the surface). This arrangement enabled high-fidelity measurements of the wall's thermal response and informed subsequent numerical modeling efforts (Figure 4).

2. Materials and Methods

2.1 Material properties

Physical and thermal properties of Amzirc and electro-formed copper are implemented as temperature dependent considering the in depth NASA characterization presented by J.J. Espoito et al.[1] Moreover, the data from J.J. Espoito et al.[1] at cryogenic (27.6 K), room (294.3 K) and high temperatures (533.1 K and 755.4 K) of monotonic-tensile tests are used to calibrate the 2nd order Chaboche hardening model for the electro-formed copper. Due to the lack of low

DOI: 10.13009/EUCASS2025-500

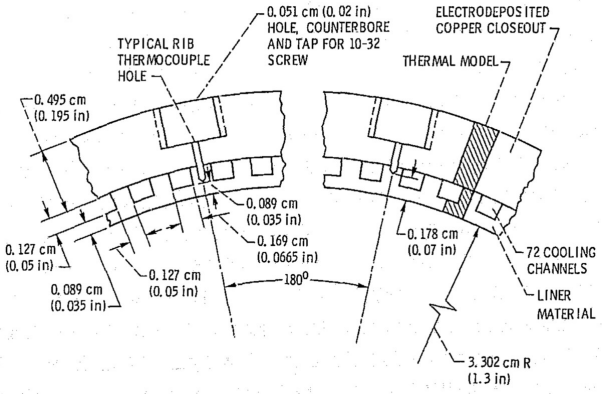

Figure 4: Cross section of the cylindrical chamber. Image from[4]

cycle fatigue data for the electro-formed copper the electro-formed copper hardening models is not only calibrated with respect to tensile curved, but also not considering the Voce isotropic model (which intricately depends on the not available cycling behavior). This assumption is considered as not critical since the electro-formed copper is employed in the close out structure of the SN40 case study combustion chamber, thus no plastic strain is expected. The available low cycle fatigue tests at room (294.3 K) and high temperature (810 K) are used to calibrate the combined 2nd order Chaboche-Voce combined hardening model for the Amzirc. Since the cryogenic (27.6 K) low cycle fatigue curves for Amzirc are not available, the coefficients have been extrapolated. The isotropic hardening is a plastic model able to replicate the hardening and softening behavior of a material, but not the Bauschinger effect. The variability of the strain over the cycles is taken into account by considering a dependency of the yield strength, in the yield function, from the accumulated plastic strain. On the other hand, kinematic hardening material models assume translation of the loading surface as a rigid body in the stress space simultaneously maintaining size, shape and orientation of the initial yield surface. Thus, this model is able to replicate the Bauschinger effect. In the present study a combined, Voce isotropic and 2nd order Chaboche kinematic model is implemented for both Amzirc and electro-formed copper with temperature dependency.

Due to the availability of experimental low-cycle fatigue (LCF) data for Amzirc, the calibration of the hardening models was performed to ensure high-fidelity replication of the material's cyclic response. The model parameters were carefully tuned to capture both the stress-strain hysteresis behavior and the evolution of material characteristics over repeated loading. Figures 5 and 6 illustrate the comparison between the experimental LCF curves and the corresponding numerical predictions at room temperature and 810 K, respectively. The results clearly demonstrate the model's ability to accurately reproduce key cyclic phenomena, including the progressive material softening and the Bauschinger effect. The numerical curves closely follow the experimental data, both in terms of the first loading cycle and the stabilized hysteresis loops, indicating a robust agreement between simulation and test. This consistency across a wide temperature range validates the reliability of the implemented constitutive model for Amzirc in representing the cyclic plasticity behavior under thermo-mechanical loading conditions.

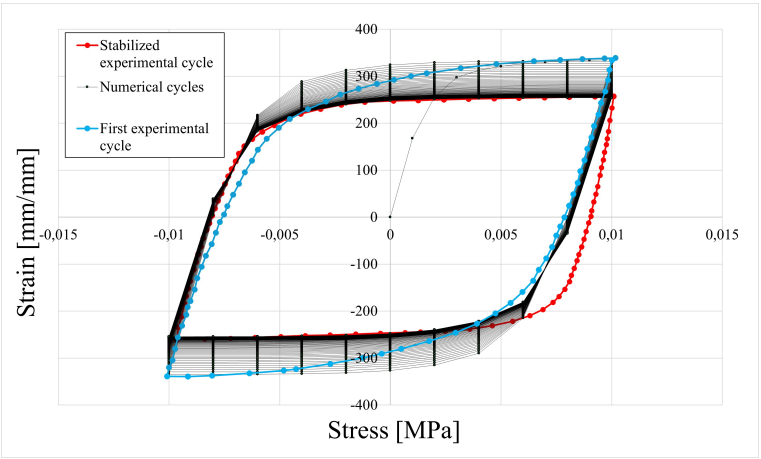

Figure 5

DOI: 10.13009/EUCASS2025-500

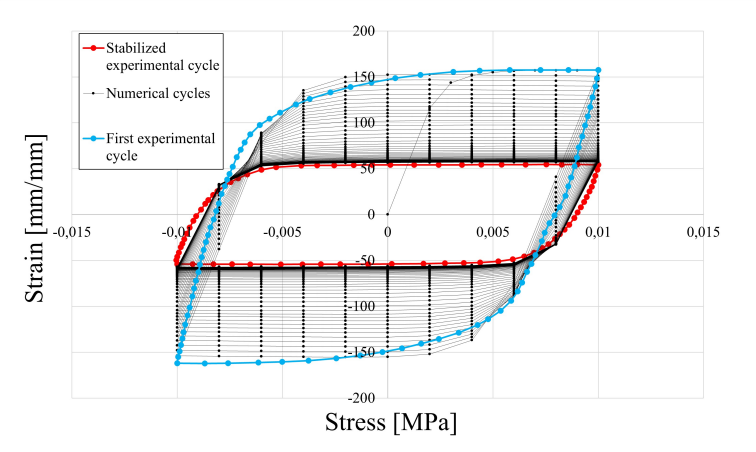

Figure 6

Although the numerical model shows overall good agreement with experimental data, a closer inspection of Figure 5 (room temperature) reveals that the predicted hysteresis loops deviate more noticeably from the experimental curves compared to the higher temperature case shown in Figure 6. Specifically, at room temperature, the numerical cycles tend to underestimate the peak tensile and compressive stresses, and do not fully capture the sharp transition zones during load reversals. These discrepancies become evident when comparing the steep portions of the loops and the corners where the Bauschinger effect is most pronounced. Both models' coefficients are presented in Table 1.

		27.6 [K]	293.4 [K]	553.1 [K]	755.4 [K]	27.6 (Note: extrapolated) [K]	293.4 [K]	810 [K]
		Electro-fromed copper				Amzirc		
Chaboche 2nd order C1	[GPa]	80	82	32	4	427	291	25
Chaboche 2nd order $\gamma 1$	[-]	1188	1697	1065	512	2559	2538	4770
Chaboche 2nd order C2	[GPa]	3	5	4	2	32	25	22
Chaboche 2nd order $\gamma 2$	[-]	3	43	43	10	388	414	906
Young's modulus [GPa]	[GPa]	118	114	109	105	230	170	58
Initial Yield stress	[MPa]	78	51	40	30	180	160	130
Voce saturation stress	[MPa]	NA	NA	NA	NA	2	2	2
Voce saturation exponent (Note: supposed)	[-]	NA	NA	NA	NA	-73	-84	-105

Table 1: Electro-formed and Amzirc hardening model coefficients.

2.2 Finite Element Method setup

The thermo-mechanical analysis conducted in this study is centered on the SN40 plug chamber experiment, specifically focusing on the throat section, the region most exposed to intense thermal and mechanical loads. A finite element model was developed to replicate the real experimental conditions and enable evaluation of material response and structural behavior under repeated thermal cycles. The simulation was carried out using a commercial finite element solver capable of handling coupled nonlinear thermal and mechanical analyses.

The computational workflow was divided into two main stages. First, a transient thermal analysis was performed using the thermal boundary conditions corresponding to a nominal firing cycle. This simulation generated a time-resolved temperature field across the structure, capturing the dynamic thermal gradients experienced during ignition, steady burn, and post-cooling phases. The resulting temperature distribution served as input for the second stage: a sequential non-linear quasi-static thermo-structural analysis conducted at multiple time points within each cycle to assess mechanical stresses and strains. In total, 40 consecutive cycles were simulated to capture the evolution of material deformation accumulation over time. Every single simulated thermo-structural cycle is characterized by the same transient thermal load and mechanical load of the previous cycle. An important aspect of the setup was the initialization of the first mechanical cycle at ambient (room) temperature to mirror the actual test procedure, thereby

DOI: 10.13009/EUCASS2025-500

accounting for the transient mechanical behavior that occurs in the early cycles due to the large thermal differential.

Calibrated thermal boundary conditions were applied to both the coolant and hot gas interfaces. For the coolant side, forced convection heat transfer coefficients and reference temperatures were imposed on each side of the rectangular cooling channels (top, bottom, and lateral walls). While each side was assigned a constant coefficient, the values varied between surfaces to reflect differences in local cooling performance. The reference temperature was taken as the bulk temperature of liquid hydrogen. On the hot gas side, the thermal boundary was modeled using heat transfer coefficients and adiabatic wall temperatures, validated by experimental data from the SN40 test article. Thus, multiple iteratively transient thermal analysis have been used to manual modify the heat exchange coefficients in order to match the numerical results with the time-dependent temperature measures taken with the immersed thermocouples (Figure 7). Although some heat conduction to the external environment occurs through the closeout layer in the real engine, this contribution was neglected in the numerical model by assuming adiabatic conditions at the outer surfaces, justified by the relatively small thermal gradient in the external regions.

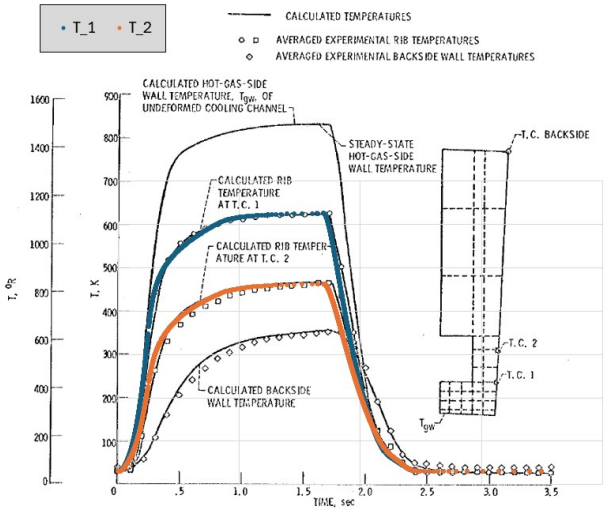

Figure 7: Experimental versus numerical wall temperature time variation of SN40 experiment.[4]

Mechanical loading are applied consistently with the different phases of the combustion cycle. All time-dependent thermal and mechanical loads were modulated using linear interpolation functions to simulate the transitions between ignition, steady-state firing, and cool-down. These functions allowed for a smooth representation of boundary condition evolution throughout each 3.5-second cycle. The full boundary condition timeline and values are summarized in Figure 9 and Table 2.

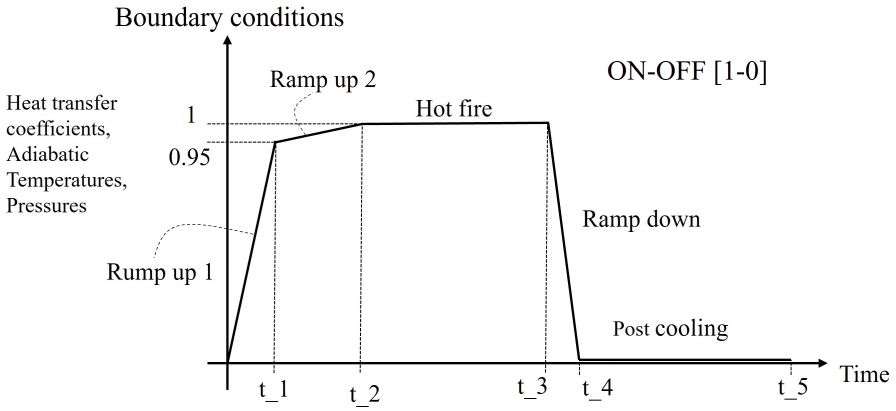

Figure 8: Numerical nominal cycle.

DOI: 10.13009/EUCASS2025-500

Variables	Unit	Ramp up 1	Ramp up 2	Hot fire	Ramp down	Post cooling
Δt	[s]	0.25	0.85	1.7	2.2	3.5
p_c	[bar]	62.2	51	65.5	51	51
p_{hg}	[bar]	26.1	27.5	27.5	1	1
p_{out}	[bar]	1	1	1	1	1
h_{hg}	[kW/m^2/K]	19	20	20	0	0
T_{hg}	[K]	3125.5	3290	3290	294	294
$h_{c,top}$	[kW/m^2/K]	152	160	160	150	150
$h_{c,lateral}$	[kW/m^2/K]	32.3	34	34	75	75
$h_{c,bottom}$	[kW/m^2/K]	32.3	34	34	75	75
T_c	[K]	54.1	57	57	29	29

Table 2: Numerical nominal cycle external loads.

The study involves 3 different half cooling channel numerical configurations:

- 2D plain strain analysis. This condition assumes no strain in the out-of-plane (axial) direction. The structure is modeled as if it were infinitely long in the axial direction. There's no axial deformation and the entire length of the domain undergoes identical deformation in the cross-section;

- 2D generalized plain strain analysis. This model assumes that axial strain is uniform, but not necessarily zero. This is achieved by constraining only the average axial strain, while allowing the model to relax or stretch in the axial direction uniformly. No gradients of axial strain are allowed (i.e., no bending or warping), but the domain can expand or contract axially. This mechanical condition has been found[5] to be more representative, with respect to the 2D plain strain condition, of the real cycling behavior of regenerative cooled thrust chamber by reducing the over strain prediction of the 3D generalized plain strain analysis and the under prediction of the 2D common plain strain numerical setup;[5]

- 3D generalized plain strain analysis. This model explicitly constrains the axial strain to remain constant, similar to the 2D Gen. PS case but in the 3D domain, allowing a full 3D resolution of the stress and strain fields. The axial z strain direction is kinematically coupled between z-normal positive and negative surfaces of the structure. This is necessary to ensure avoid a non-realistic fully free z axial deformation;

The computational mesh for the 2D numerical configurations was composed of 903 quadrilateral 4-nodes linear elements and 1,990 nodes, using a non-structured topology. On the other hand, the 3D numerical configuration involved 903 hexahedron 8-nodes linear elements, for a total of 3980 nodes. The average element size was fixed at approximately 0.1 mm, chosen to ensure adequate resolution across the inner wall width and to match the half channel's 3D axial thickness in the 3D generalized plain strain analysis. This high spatial fidelity was critical for capturing steep thermal gradients and localized plastic deformation, especially near the hot gas wall side.

Material behavior was modeled as nonlinear and temperature-dependent for both the Amzirc liner and electro-formed copper closeout. The finite element solver was configured to account for large deformations, plasticity, and nonlinear material properties. The hardening models involved in the present study is a combined non linear kinematic hardening 2nd order Chaboche models combined with a multi-linear isotropic hardening Voce model.

Geometric and mechanical constraints were carefully chosen to replicate the experimental boundary conditions. A rotational symmetry condition was enforced along the two r-z symmetry planes of the modeled half-chamber segment to account for axis-symmetry. The out of plain surface (normal with respect to the z axis) of the structure was fixed in the axial direction (uz = 0). If the 2D plain strain and generalized plain strain conditions are applied directly with an option in the commercial structural solver, for the 3D generalized plain strain analysis the nodes on surface normal with respect to the negative z axis were hard coded to be coupled in the z-direction together with the surface normal with respect to the positive z axis. This coupling established a generalized plane strain condition, ensuring that axial displacements were consistent across symmetry z axis plane.

DOI: 10.13009/EUCASS2025-500

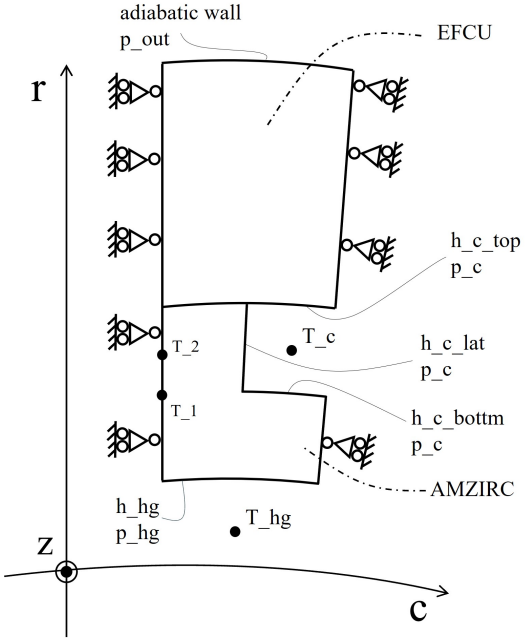

Figure 9: Mechanical and thermal boundary conditions scheme.

2.3 Life prediction

The fatigue life of the inner wall the regenerative-cooled SN40 Plug Chamber was predicted using a cycle-by-cycle cumulative damage model, according with the Miner's damage rule. The model accounts for both low-cycle fatigue (LCF) and ratcheting effects under thermo-mechanical loading. For each load cycle i, the total hoop (circumferential direction) strain range, denoted as $\Delta\varepsilon_{hoop} = \varepsilon_{hoop,max_{cycle\ i}} - \varepsilon_{hoop,min_{cycle\ i}}$, was used as the input to the Coffin-Manson experimental curve at 810 K[1] relation to estimate the number of cycles to failure $N_{f_{LCF}}$:

$$\Delta\varepsilon_{hoop} = \varepsilon'_f(2N_{f_{LCF}})^c$$

where:

- ε'_f is the fatigue ductility coefficient, and equal to 67,76;
- c is the fatigue ductility exponent, and equal to -0,487;

The LCF damage per cycle was calculated using Miner's rule as:

$$D_{\mathrm{LCF},i} = \frac{1}{N_{f_{LCF},i}}$$

The cumulative fatigue damage over n cycles is:

$$D_{\mathrm{LCF,total}} = \sum_{i=1}^{n} D_{\mathrm{LCF},i}$$

Ratcheting damage was assessed by evaluating the progressive total (elastic and plastic) hoop tensile strain accumulation at the end of each cycle, thus after the shout down phase, according with J. Riccius et al.[5] :

$$\Delta\varepsilon_{\mathrm{hoop,ratchet},i} = \varepsilon_{hoop,\mathrm{end},i+1} - \varepsilon_{hoop,\mathrm{start},i}$$

The ratcheting damage per cycle was calculated as follow:

$$D_{\mathrm{ratchet},i} = \frac{max(0, \Delta\varepsilon_{\mathrm{hoop,ratchet},i})}{\varepsilon_{\mathrm{max,tensile}}}$$

where:

DOI: 10.13009/EUCASS2025-500

- $\varepsilon_{\text{max,tensile}}$ is the elongation to fracture of the tensile test at room temperature and equal to 0.25 mm/mm;

The cumulative ratcheting damage was given by:

$$D_{\text{ratchet,total}} = \sum_{i=1}^{n} D_{\text{ratchet},i}$$

The total damage per cycle is the sum of both LCF and ratcheting contributions:

$$D_{\text{total},i} = D_{\text{LCF},i} + D_{\text{ratchet},i}$$

The cumulative usage factor is:

$$D_{\text{cumulative}} = \sum_{i=1}^{n} D_{\text{total},i}$$

Failure was predicted when at lease one point of the structure satisfies the following criteria:

$$D_{\text{cumulative}} \geq 1$$

3. Results and discussion

The results generally exhibit the classical thinning of the inner wall, leading to the characteristic "dog-house effect" (Figure 10). The critical location selected for fatigue life prediction and thermo-mechanical behavior analysis of the SN40 Plug Chamber is referred to as Point A, identified in Figure 11 and Figure 12.

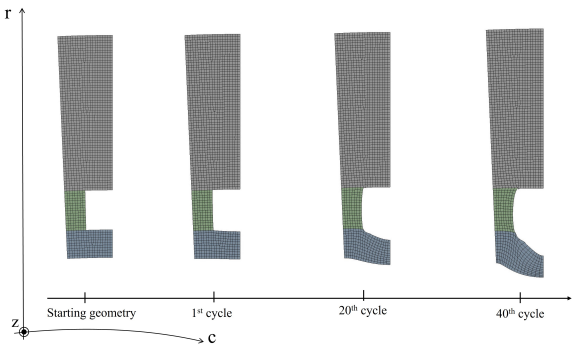

Figure 10: General deformation of the combustion chamber regenerative cooling half channel at different cycles

Point A corresponds to the mid-section of the inner wall on the hot-gas side, which is subjected to the highest thermal loads and strain amplitudes during engine firing cycles. This selection is further supported by consistent experimental observations (Figure 1), which confirm the appropriateness of evaluating the life of regenerative cooling structures at this location. However, it is important to note that Point A does not correspond to the numerically highest-stressed region. According to the simulation results and literature findings,[2,6] the maximum computed stress is observed at Point B (Figure 12), which is located near a geometric discontinuity, typically a corner or edge. This localized overestimation is commonly attributed to finite element method (FEM) singularities and stress concentration effects that are often exaggerated at mesh corners. Furthermore, elemental distortion and mesh degradation due to large cyclic deformations at Point B compromise the accuracy and reliability of long-term simulations in that region. Despite exhibiting higher strain magnitudes, Point B is considered a localized effect-its elevated stress and strain states are restricted to a small number of elements and do not propagate spatially with continued cycling. In contrast, Point A displays a more distributed deformation pattern. Over successive cycles, the high strain field at Point A expands in both the circumferential and radial directions, involving a broader mesh region. This behavior aligns more closely with crack initiation and propagation mechanisms, as supported by fracture mechanics theory. For this reason, Point A was selected as the reference location for fatigue life prediction in the regenerative-cooled chamber simulations.[2,6]

DOI: 10.13009/EUCASS2025-500

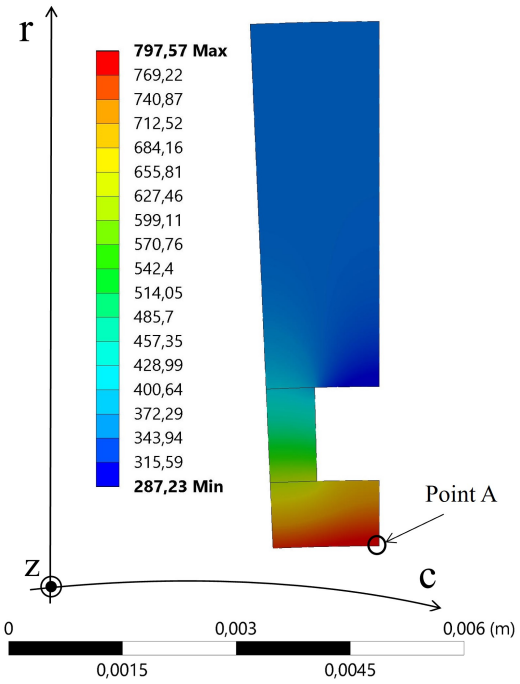

Figure 11: Temperature distribution at the hot firing phase.

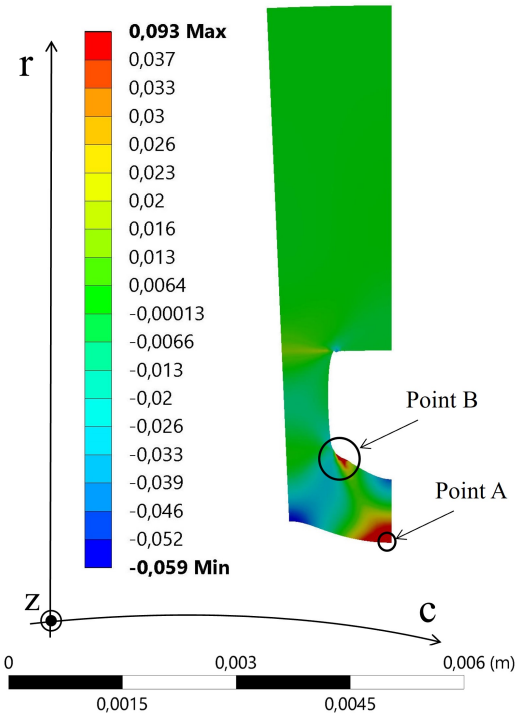

Figure 12: Representative example of hoop elastic and plastic strain distribution at the 40th cycle hot fire phase - 2D plain strain model

The evolution of the maximum equivalent total strain at Point A over 40 cycles is presented in Figure 13. A distinct transient behavior is observed in the first 5-10 cycles, followed by a stabilization regime. The 2D generalized plain strain (2D Gen. PS) model stabilizes the fastest and exhibits the lowest residual equivalent strain amplitude, stabilizing around 0.0025, compared to 0.0105 for 2D plain strain (2D PS) and 0.009 for 3D generalized plain strain (3D Gen. PS). The reduced equivalent strain in the 2D generalized plain strain model indicates lower plastic dissipation

DOI: 10.13009/EUCASS2025-500

per cycle, which directly correlates with a slower damage accumulation. This result underscores the strain-constraining effect of the generalized plain strain boundary conditions, which more realistically replicate the axial continuity and stiffness of the full chamber wall in the engine.

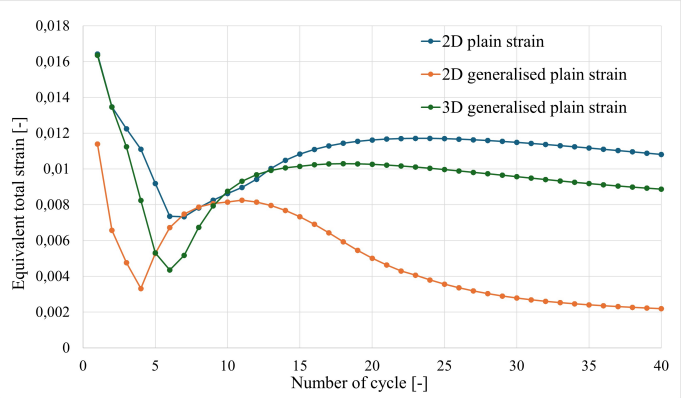

Figure 13: Comparison of the maximum equivalent total strain at Point A over cycles for different numerical models.

The time history of Point A hoop elastic and plastic strain over multiple thermal cycles is presented in Figure 14. The 3D Gen. PS model accumulates the highest level of plastic hoop strain, exceeding 0.065 mm/mm, indicating significant progressive ratcheting. Conversely, the 2D Gen. PS model saturates near 0.038 mm/mm, confirming a strongly constrained ratcheting response. This behavior directly impacts the damage calculation since the ratcheting component is dominant in thermo-mechanical fatigue under these loading conditions. This trend is further validated by the cyclic stress-strain hysteresis curves (Figures 15-17), which illustrate the hoop stress versus hoop elastic and plastic strain over consecutive cycles. The 2D PS model shows wide hysteresis loops and a progressive rightward shift, typical of ratcheting-dominated behavior. The 2D Gen. PS model, in contrast, shows narrower loops with a nearly closed profile after initial cycles, confirming stabilization. The 3D Gen. PS loops are intermediate in width but show more pronounced ratcheting than the 2D Gen. PS case, reinforcing the idea that the axial constraint is critical to controlling plastic strain accumulation.

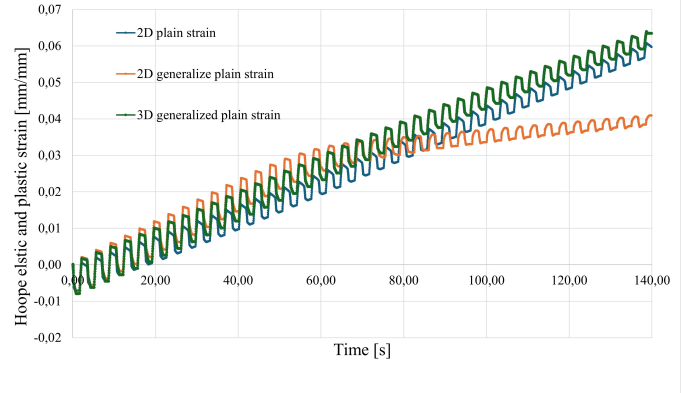

Figure 14: Hoop plastic and elastic strain over time at Point A for different numerical models.

DOI: 10.13009/EUCASS2025-500

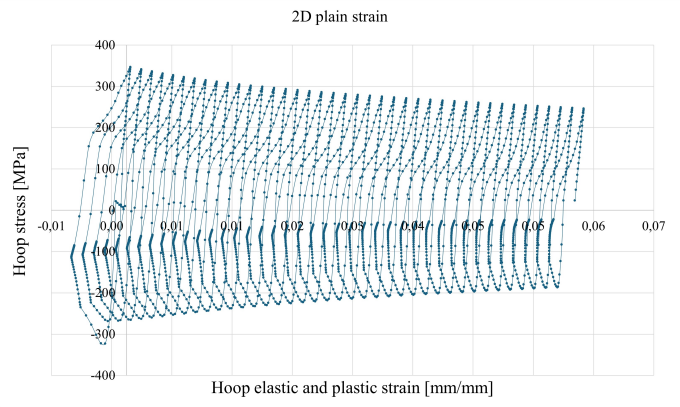

Figure 15: Hoop elastic and plastic strain vs hoop stresses at Point A - 2D plain strain model.

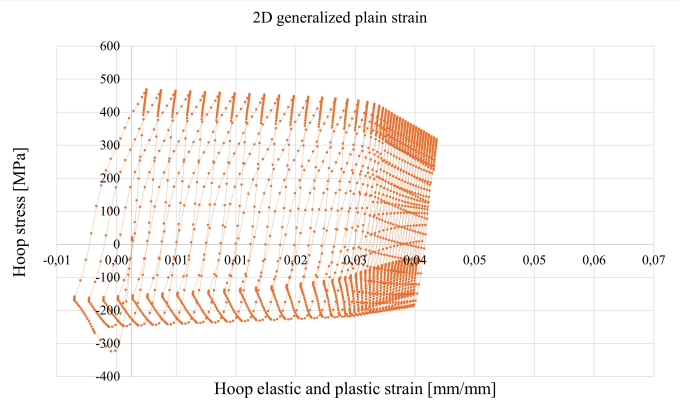

Figure 16: Hoop elastic and plastic strain vs hoop stresses at Point A - 2D generalized plain strain model.

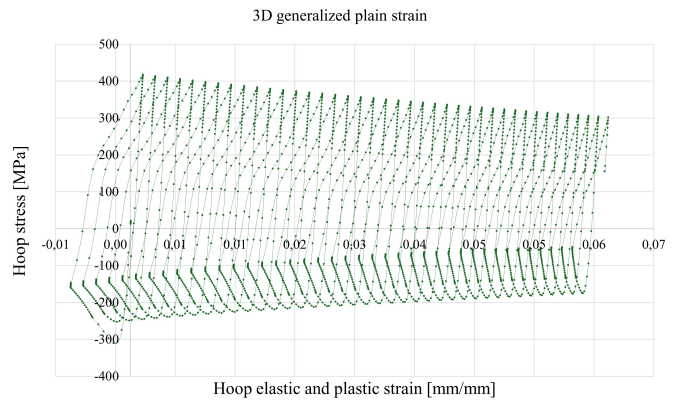

Figure 17: Hoop elastic and plastic strain vs hoop stresses at Point A - 3D generalized plain strain model.

Figure 18 presents the cumulative damage evolution as a function of the number of cycles. For each model, the total damage was computed using a linear damage summation approach (Palmgren-Miner rule), incorporating both low-cycle fatigue (LCF) and ratcheting damage mechanisms. The 2D PS simulation predicts failure after approximately 150 cycles, while the 3D Gen. PS simulation yields a similar prediction around 140-145 cycles. In contrast, the 2D Gen. PS model significantly extends the predicted fatigue life to about 570 cycles, with the damage threshold $D = 1$ being reached much later. The experimental failure of specimen SN40 occurred at 390 cycles, marked in the graph with a red cross. Notably, the extrapolated linear damage from the 2D Gen. PS model intersects the critical damage threshold closer to the experimental point compared to the other models. The 2D PS and 3D Gen. PS models under-predict the fatigue life, with a relative error exceeding 60%, suggesting they overestimate damage accumulation.

DOI: 10.13009/EUCASS2025-500

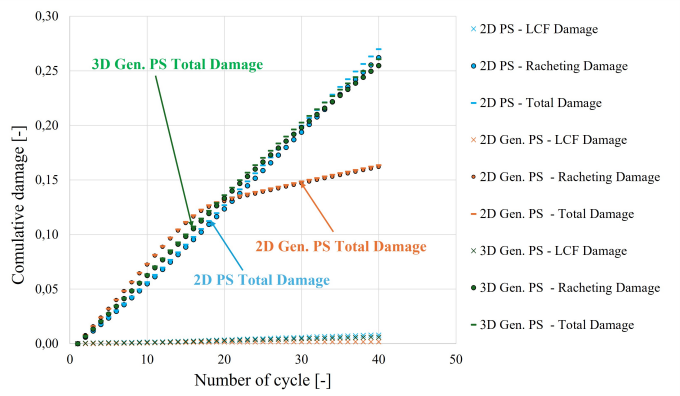

Figure 18: Low cycle fatigue damage contribution, ratcheting damage contribution and total damage at Point A for different numerical models.

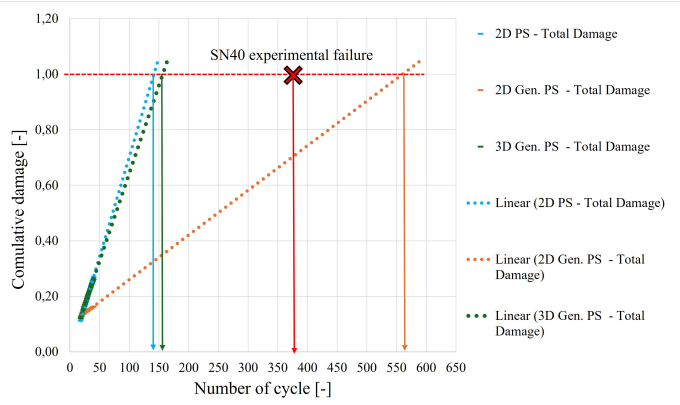

Figure 19: Total damage extrapolation at Point A for different numerical models.

Figure 18 provides a decomposition of the total damage into low-cycle fatigue (LCF) and ratcheting components. For all three models, LCF damage remains negligible (<0.01) across the entire simulated range, while ratcheting is the dominant mechanism. The 2D PS and 3D Gen. PS models show nearly identical total damage progression, reaching 0.25 at 40 cycles, while the 2D Gen. PS model accumulates only 0.13 over the same range.

The significant variation in life prediction across the different modeling approaches can be primarily attributed to the way out-of-plane constraint and structural stiffness are represented. The 2D plain strain model artificially enforces zero axial strain, leading to an overly stiff response that is not properly representative of the actual loading environment, which permits some axial relaxation. The 3D model,while offering full geometric fidelity, was constrained to enforce a constant axial strain across the domain, mimicking the 2D Generalized Plain Strain condition. Despite this realistic constraint, the 3D formulation still exhibited slightly ratcheting accumulation compared to the 2D Gen. PS model, likely due to the fully resolved three-dimensional stress interactions and degrees of freedom that allow for more complex local deformation modes within the structure. This results in conservative (i.e., short) life predictions. The 2D generalized plain strain model, however, captures a more realistic intermediate behavior by constraining axial strain based on average stiffness while avoiding full fixity. As such, it offers a computationally efficient and physically reasonable approximation, especially for axisymmetric, axially continuous structures like rocket engine throat section cooling channels. The strong correlation between the 2D Gen. PS prediction and the experimental SN40 failure point (390 cycles) suggests that this modeling approach achieves an optimal balance between accuracy and computational cost. In contrast, the 2D PS and 3D Gen. PS models are either too constrained or too relaxed, respectively, leading to over-prediction of damage accumulation and premature failure estimation.

Although the 3D Gen. PS model incorporates full three-dimensional geometry, ratcheting is computed only in the hoop direction, which aligns with the primary loading axis of the cylindrical thrust chamber.

Despite this directional focus, the 3D setup leads to additional deformation modes that affect the hoop response indirectly. This is mainly attributed to the redistribution of stress and strain in the cross-section, amplifying the hoop plastic strain response. As a result, the hoop ratcheting is overestimated. This leads to an artificially high accumulation

DOI: 10.13009/EUCASS2025-500

of permanent strain in the hoop direction, thereby accelerating damage prediction, even though ratcheting is only computed in one direction. In contrast, the 2D Generalized Plane Strain model mimics the real constraint more effectively by forcing the average axial strain to stay constant, which reduces this unphysical ratcheting effect and gives a more accurate life prediction.

4. Conclusions

This study investigated the influence of different numerical modeling assumptions on the thermo-mechanical fatigue life prediction of a regenerative-cooled liquid rocket engine (LRE) combustion chamber. By simulating 40 firing cycles of the SN40 Plug Chamber using three finite element (FE) formulations-2D plain strain (2D PS), 2D generalized plain strain (2D Gen. PS), and 3D generalized plain strain (3D Gen. PS), it was possible to evaluate the mechanical response and cumulative damage accumulation under realistic thermal and mechanical loading.

The simulations revealed that the choice of strain assumption plays a dominant role in fatigue life prediction, due to its direct impact on the development of hoop total strain and ratcheting. While the 2D PS and 3D Gen. PS models predicted early failure after approximately 150 and 140 cycles respectively, the 2D Gen. PS model extended life up to 570 cycles, showing the best agreement with the experimental failure of the SN40 chamber at 390 cycles.

The difference in predictions was traced to the representation of axial constraints. The 2D PS model imposed excessive rigidity, limiting axial deformation unrealistically and leading to overestimated strain concentrations. The 3D Generalized Plain Strain avoided the overestimated ratcheting typically seen in fully unconstrained 3D simulations. Nevertheless, due to the fully resolved stress and strain fields in three dimensions, the model exhibited higher ratcheting accumulation than its 2D counterpart, resulting in a somewhat more conservative fatigue life prediction. The 2D Gen. PS model offered a more realistic balance by approximating the axial constraint observed in the actual chamber geometry, thus better capturing the progressive deformation and damage mechanisms.

The study also demonstrated that ratcheting, rather than classical LCF, is the dominant failure mechanism in such structures, as observed in the decomposed damage plots.

Finally, Point A, located at the mid-thickness of the inner wall on the hot-gas side, was confirmed as the appropriate location for life assessment. Although Point B showed higher localized stress and strain magnitudes, it was subject to corner effects, mesh distortion, and did not exhibit a spatially propagating damage field. In contrast, Point A presented distributed damage consistent with known crack propagation paths in similar structures.

5. Acknowledgments

The authors gratefully thank ASI (Italian Space Agency) for financial support of PhD research activity which lead to the present results.

References

[1] Esposito. Thrust chamber life prediction - Volume 1 Mechanical and physical properties of high performance rocket nozzle materials.

[2] Di Liu, Bing Sun, Taiping Wang, Jiawen Song, and Jianwei Zhang. Thermo-structural analysis of regenerative cooling thrust chamber cylinder segment based on experimental data. *Chinese Journal of Aeronautics*, 33(1):102–115, January 2020.

[3] Marco Pizzarelli. An Algebraic Model for Structural and Life Analysis of Regeneratively-Cooled Thrust Chambers. *Journal of Propulsion and Power*, 36(2):191–201, March 2020.

[4] R.J. Quentmeyer. Experimental Fatigue Life Investigation of Cylindrical Thrust Chambers.

[5] Joerg Riccius, Malte Hilsenbeck, and Oskar Haidn. Optimization of geometric parameters of cryogenic liquid rocket combustion chambers. *37th Joint Propulsion Conference and Exhibit*, July 2001.

[6] Joerg R. Riccius, Quentin Wargnier, Wissam Bouajila, and Evgeny B. Zametaev. Inner liner temperature variation caused deformation localisation effects in a multichannel model of a generic LRE wall structure. In *50th AIAA/ASME/SAE/ASEE Joint Propulsion Conference*, Cleveland, OH, July 2014. American Institute of Aeronautics and Astronautics.